


Article

Creep Rate, Friction, and Wear of Two Heat-Affected Zone Regions of 9–12 wt.% Cr Steels

Igor Velkavrh ^{1,*} , Joël Voyer ¹ , Fevzi Kafexhiu ²  and Bojan Podgornik ²¹ V-Research GmbH, Stadtstrasse 33, 6850 Dornbirn, Austria; joel.voyer@v-research.at² Institute of Metals and Technology, Lepi pot 11, 1000 Ljubljana, Slovenia; fevzi.kafexhiu@imt.si (F.K.); bojan.podgornik@imt.si (B.P.)

* Correspondence: igor.velkavrh@v-research.at; Tel.: +43-55-7239415928

Abstract: Coarsening of precipitates can have a profound effect on the mechanical properties of martensitic 9–12 wt.% Cr steels, which are typically used in critical parts of fossil-fuel power plants such as turbines, headers, and main steam pipes. In the present study, changes in precipitates' size and distribution in the simulated heat-affected zone of two different 9–12 wt.% Cr steels (X20 and P91) after different aging conditions were analyzed and correlated with their creep, friction, and wear behaviors. It was shown that prior to aging, the morphology of the steel matrix (prior austenite grain size and microstructure homogeneity) governed the creep rate and the tribological performance of both steels, while after aging their response was additionally determined by the combination of the number and the size of precipitates. For the selected samples (prepared under identical conditions), number of precipitates was found to be within a narrower range for the X20 steel as compared to the P91 steel. For both steels, aging for a shorter time at the higher temperature yielded significantly higher stationary creep rate values as compared to aging for longer time at the lower temperature. The increase was more pronounced in the P91 than in the X20 steel. Both prior to and after aging, the P91 steel typically provided slightly higher creep resistance than the X20 steel, while the latter provided slightly better tribological performance. Furthermore, as a function of the increasing number of precipitates, static coefficient of friction in air atmosphere was approximately linearly decreasing, while the wear rate initially decreased.

Keywords: 9–12 wt.% Cr steels; precipitates; creep; friction; wear

Citation: Velkavrh, I.; Voyer, J.; Kafexhiu, F.; Podgornik, B. Creep Rate, Friction, and Wear of Two Heat-Affected Zone Regions of 9–12 wt.% Cr Steels. *Metals* **2021**, *11*, 558. <https://doi.org/10.3390/met11040558>

Academic Editors: Irina P. Semenova and Kohichi Sugimoto

Received: 22 December 2020

Accepted: 15 March 2021

Published: 29 March 2021

Publisher's Note: MDPI stays neutral with regard to jurisdictional claims in published maps and institutional affiliations.



Copyright: © 2021 by the authors. Licensee MDPI, Basel, Switzerland. This article is an open access article distributed under the terms and conditions of the Creative Commons Attribution (CC BY) license (<https://creativecommons.org/licenses/by/4.0/>).

1. Introduction

Due to their excellent mechanical properties, corrosion resistance at elevated temperatures and good machinability, 9–12 wt.% Cr martensitic creep-resistant steels are used in critical parts of fossil-fuel power plants, such as turbines, headers, main steam pipes, etc. [1–4]. At high temperatures and under static loading conditions under which the 9–12 wt.% Cr steels are mostly used; creep is the main deteriorating mechanism. Consequently, the majority of research on 9–12 wt.% Cr steels has been focused on their creep resistance [5–9]. However, 9–12 wt.% Cr steels are also used for steam turbine blades [10]; therefore, understanding of their mechanical and tribological behaviors under dynamic loading conditions is very important [3]. Very little information in this regard can be found in the available literature. Nevertheless, for 9–12 wt.% Cr steels, fatigue resistance under the influence of corrosion pits [11], as well as under fretting conditions [12], was already analyzed.

The creep behavior of real and simulated welds in 9–12% Cr steels with a special emphasis on the HAZ has been a subject of extensive investigations [13–21]. Welding is a common technique applied for the assembly of large complex structure components of thermal power units. Due to rapid heating and cooling during welding, non-equilibrium microstructures are formed in the heat-affected zone (HAZ), a narrow zone of parent metal adjacent to the weld fusion line altered by the weld thermal cycle, leading to the

degradation of its mechanical properties and weakening of the entire welded joint [22,23]. Therefore, the HAZ is often regarded as the weakest link in welded constructions.

After welding, precipitates with different size, spacing, and distribution are present in the HAZ. Various studies [6,24–27] have shown that there is a correlation between the size, spacing, and distribution of these precipitates on one hand and creep properties on the other. In addition, other microstructural features such as dislocation structure and evolution [8,28–30], subgrain structure [31–33], and the formation of secondary phase particles, such as Laves phase or Z-phase [15,34,35], play a pivotal role on the performance of these materials, especially at long-term creep conditions. In previous studies of the present authors, it was also observed that by aging, improved wear resistance is achieved due to precipitation strengthening by finely dispersed carbides and nitrides [36]. On the other hand, friction of the aged samples was higher as compared to the non-aged ones, which was true for both air and Ar atmospheres [37].

In the present study, the results of creep tests, friction, and wear of the parent metal and the simulated HAZ of two grades of 9–12 wt.% Cr steels are analyzed and compared from the viewpoint of the number, size, and spacing of precipitates, as a function of isothermal aging at 650 °C for 17,520 h and at 750 °C for 4320 h. We presume that precipitates' size and distribution predominantly change with the chosen aging times and temperatures, and that these changes indirectly reflect the evolution of the substructure (martensite laths) and dislocations' structure, while no significant change in prior austenite grain (PAG) size takes place.

2. Materials and Methods

2.1. Materials and Microstructures

Two grades of creep-resistant 9–12 wt.% Cr steels, X20 (DIN X20CrMoV121) and P91 (DIN X10CrMoVNb91), were used in this study. In Table 1, chemical composition of both steels obtained by optical emission spectrometry (OES) is given. For wear and friction experiments, cylindrical samples with a diameter of 13 mm were used. Samples were initially austenitized at 1050 °C for 30 min to dissolve the precipitates in austenite. Afterwards, samples were quenched in oil, resulting in a brittle and hard martensitic microstructure. Finally, standard tempering procedure at 810 °C for 30 min was performed and followed by air cooling, resulting in a tempered martensitic microstructure, which represented the basis (parent metal, α) for further heat treatment processes.

Table 1. Chemical composition of X20 and P91 steels.

Element	X20 (wt.%)	P91 (wt.%)
C	0.20	0.10
Si	0.29	0.38
Mn	0.52	0.48
P	0.019	0.012
S	0.011	0.002
Cr	11.0	7.9
Ni	0.64	0.26
Mo	0.94	0.98
V	0.31	0.23
Cu	0.059	0.14
Nb	0.024	0.11
Al	0.032	0.016
N	0.017	0.064

To simulate two different HAZ regions, i.e., inter-critical ($\alpha + \gamma$) and coarse-grained (γ) microstructures, additional heat treatment procedures were performed. The $\alpha + \gamma$ microstructure was obtained by keeping the samples in the temperature range of $Ac1 < T < Ac3$, i.e., at 845 °C, for 60 min, where $Ac1 \approx 837$ °C and $Ac3 \approx 903$ °C represent the beginning and the end of α to γ transformation, respectively [16]. The γ microstructure

was obtained by keeping the samples above the Ac_3 temperature, i.e., at $1000\text{ }^\circ\text{C}$, for 30 min. To complete the HAZ simulation, the samples were rapidly cooled in air. The reason for keeping the samples at simulation temperatures for 30 and 60 min in comparison to the real weld HAZ, where the heating and cooling is completed in seconds, is to make sure that the target simulating temperature would be achieved throughout the whole sample of dimensions $100 \times 200 \times 200\text{ mm}^3$, from which specimens for creep and tribological tests were machined.

The γ represents the coarse-grained microstructure as it is obtained at $1000\text{ }^\circ\text{C}$ ($T > Ac_3$), being high enough for complete austenitization and grain growth. The $\alpha + \gamma$ represents the inter-critical region with fine grains because at $845\text{ }^\circ\text{C}$ ($Ac_1 < T < Ac_3$), a partial austenitization takes place along the boundaries of α grains, where γ grains begin to form, resulting in a two-phase microstructure. In other words, at these conditions, a sort of balance between the ferritic (tempered martensitic) and austenitic microstructure coexists, which on cooling transforms back to martensite. As a measure of a successful HAZ simulation, qualitative evaluation of the difference in the PAG size was applied. For this purpose, samples were ground, polished, and finalized by colloidal silica emulsion polishing (OPS) for the electron backscatter diffraction (EBSD) analysis using JEOL JSM-6500F (JEOL Ltd., Tokyo, Japan) scanning electron microscope (SEM) with an HKL Nordlys II EBSD camera operated by Channel5 software (Oxford Instruments HKL, Hobro, Denmark). The instrument was operated at an accelerating voltage of 15 kV, a probe current of 1.3 nA, and a tilt angle of 70° . Detection was set to 5–7 Kikuchi bands with 4×4 binning. A mapping area of $310 \times 251\text{ }\mu\text{m}^2$ and a step size of $0.4\text{ }\mu\text{m}$ were applied. Minimal post-processing was performed using ATEX software [38], as it was limited to interpolating the unindexed pixels and removing the so-called “wild spikes”. According to Altendorf et al. [39], a direct estimation of PAG boundaries using EBSD grain boundary disorientation maps, as shown in Figure 1, was performed by applying a grain boundary disorientation in the range of $15\text{--}50^\circ$.

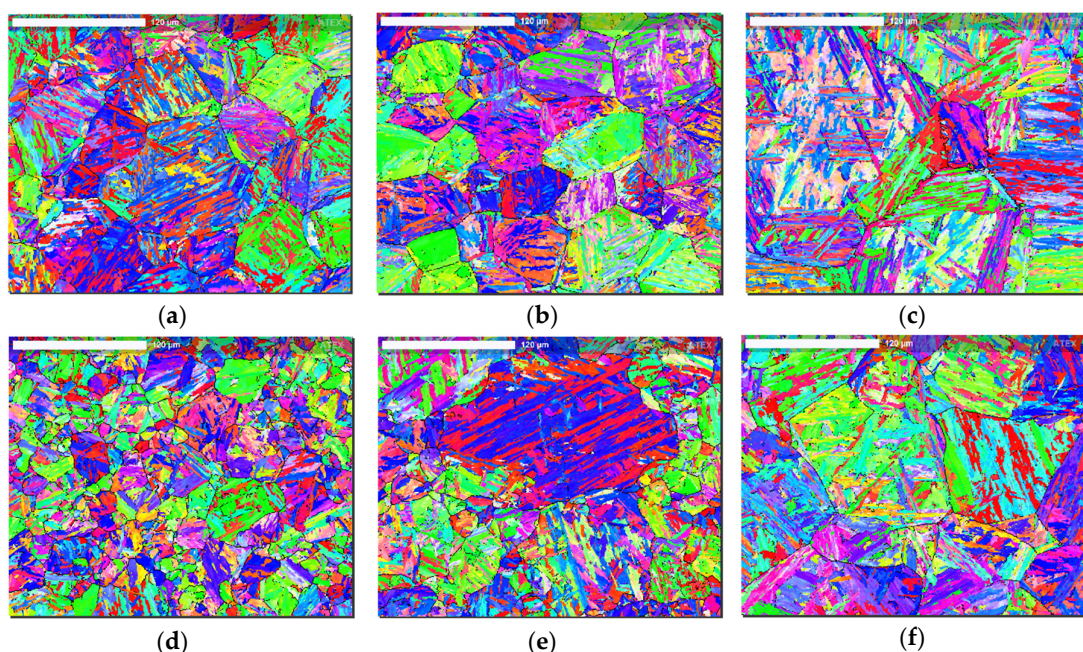


Figure 1. Electron backscatter diffraction (EBSD) inverse pole figure (IPF) with black-line denoted grain disorientation maps in the range $15\text{--}50^\circ$ revealing the prior austenite grain (PAG) boundaries for: (a) $\alpha + \gamma$, (b) α , and (c) γ microstructures of the steel X20; and (d) $\alpha + \gamma$, (e) α , and (f) γ microstructures of the steel P91.

After simulating the HAZ, the final part of the heat treatment process was performed to induce changes of size, distribution, and mutual spacing of carbide/nitride precipitates. It consisted of aging of $\alpha + \gamma$ and γ microstructures of both steels for 168 and 720 h (1 week

and 1 month) at 650 °C and 750 °C, and additionally for 4320 h (6 months) at 750 °C and 17,520 h (2 years) at 650 °C.

After the heat treatments, samples were longitudinally cut to obtain flat surfaces for microstructure characterization, friction, and wear tests. Samples were first ground with silicon carbide paper to a sufficient depth to remove any unrepresentative surface and then polished in several steps to achieve a mirror finish (surface roughness of $R_a < 0.01 \mu\text{m}$).

2.2. Carbide and Nitride Precipitation

Changes in precipitates due to aging were evaluated via the analysis of micrographs obtained with JEOL JSM-6500F (JEOL Ltd., Japan) scanning electron microscope (SEM). In order to obtain the number, average spacing, and size values of precipitates, SEM micrographs were modified with GIMP software [40] by applying a single-colored over-painting of precipitates as shown in Figure 2. The modified SEM micrographs were then analyzed using automatic image analysis in FIJI (ImageJ) software [41], with an appropriate size filter and color threshold. The SE images chosen for the analysis were acquired at magnifications of 10–30 k, for the image analyses to be both statistically representative and, from the particles size point of view, as accurate as possible. The smallest particle that could be accurately measured this way was around $0.02 \mu\text{m}$. From such analyses, the surface area and distribution (x and y coordinates) of each precipitate could be obtained. The mean interparticle spacing was evaluated by defining the nearest neighbor for each particle separately, calculating the respective center-to-center distance (λ_i) of each nearest particle couple, and finally calculating the average value (λ), as explained in [26].

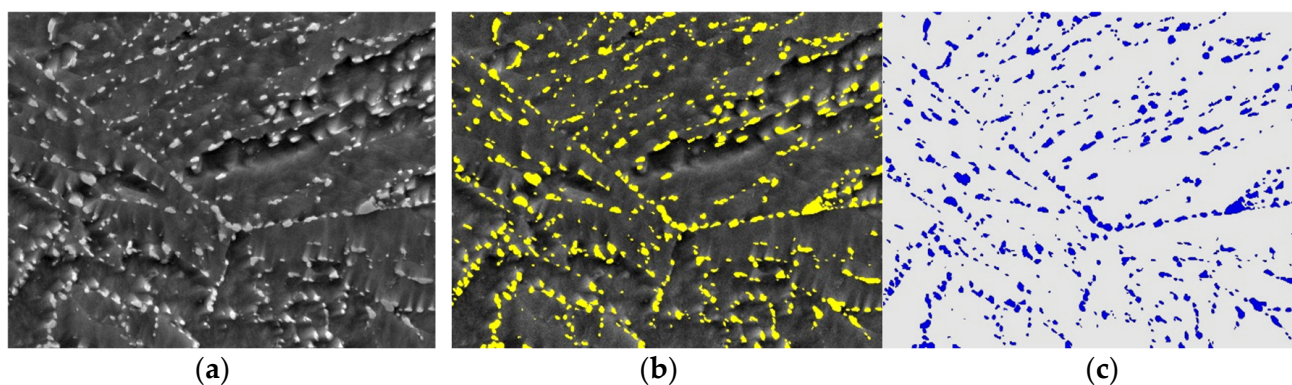


Figure 2. An example of image modification using GIMP and FIJI software: (a) SEM micrograph of precipitates, (b) SEM micrograph with a single-colored over-painting of precipitates, (c) single-colored representation of precipitates without the SEM micrograph.

SEM micrographs of the $\alpha + \gamma$ (Figure 3) and γ (Figure 4) HAZ microstructures of X20 and P91 steels for are shown for initial state, after tempering for 720 h at 650 °C, and after tempering for 720 h at 750 °C. In Figures 3 and 4, in X20 steel, a higher amount of carbide particles with more uniform distribution was observed than in P91 steel, which was true for both HAZ microstructures and for both tempering temperatures. A more detailed analysis of the SEM micrographs can be found in a previous study of the authors [36].

In Figures 5 and 6, the number of precipitates per μm^2 and their average spacing are presented for three different microstructures in their initial state and after aging under different conditions. In Figures 5 and 6, on the x-axis, aging time and/or temperature are increasing from left to right. For the α microstructure, the number and average spacing of precipitates were measured only for the initial state and after aging for 4320 h at 750 °C and for 17,520 h at 650 °C (the last two points in the diagrams in Figures 5 and 6, while for $\alpha + \gamma$ and γ microstructures the measurements were also performed after aging for 168 and 720 h at 650 and 750 °C.

In Figure 5, after aging for 168 h at 650 °C, the number of precipitates for $\alpha + \gamma$ and γ microstructures of both steels increased in comparison with the initial state. However, with increasing aging time and/or temperature, the number of precipitates started to decrease due to precipitates coarsening. For both microstructures, the lowest number of precipitates was observed after aging for 4320 h at 750 °C. Since after aging for 17,520 h at 650 °C the number of precipitates was higher, it can be concluded that at lower aging temperature, the coarsening rate of precipitates was lower, resulting in a higher number of precipitates even after significantly longer aging time. However, for the P91 steel, when aging at 650 °C, an increase in the number of precipitates as compared with the initial state was observed after the longest aging time of 17,520 h (for $\alpha + \gamma$ and γ microstructures, the number of precipitates was even higher than for the initial state), indicating that possibly, during longer aging times, an additional precipitation occurs.

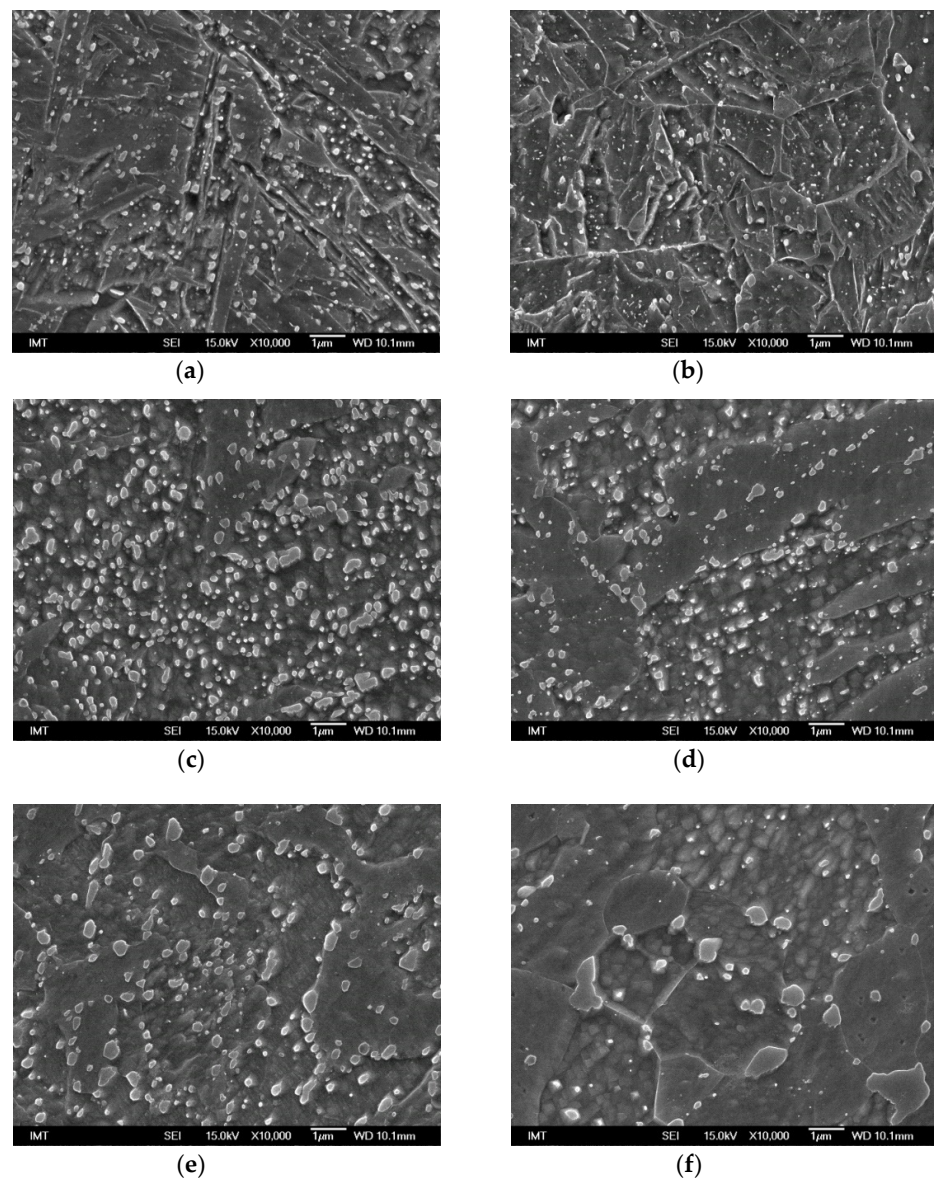


Figure 3. SEM micrographs of the inter-critical ($\alpha + \gamma$) heat-affected zone (HAZ) microstructures of X20 and P91 steels for (a,b) initial state, (c,d) after tempering for 720 h at 650 °C, (e,f) after tempering for 720 h at 750 °C. Micrographs were previously published by the present authors in [36].

For both steels, the aging-induced precipitation was more pronounced for $\alpha + \gamma$ than for γ microstructure. Therefore, after aging, the number of precipitates for $\alpha + \gamma$ microstruc-

ture was typically higher as compared to the initial state, while for γ microstructure it was typically lower as compared to the initial state. For α microstructure of both steels, the number of precipitates after aging was lower than in the initial state; however, for the X20 steel the lowest number of precipitates was measured after aging for 17,520 h at 650 °C, while for the P91 steel after aging for 4320 h at 750 °C.

In Figure 5, the average spacing of precipitates is somehow inversely correlated to the number of precipitates. The Ostwald ripening, i.e., growth of larger precipitates on the account of dissolution of smaller ones was also observed. This effect was promoted with aging temperature and time. A detailed analysis of microstructural changes was already presented elsewhere [26,36,37]. Note that the error bars in Figure 6 represent the distribution of precipitates, i.e., the smaller the error bar, the more uniform the distribution of precipitates and vice versa.

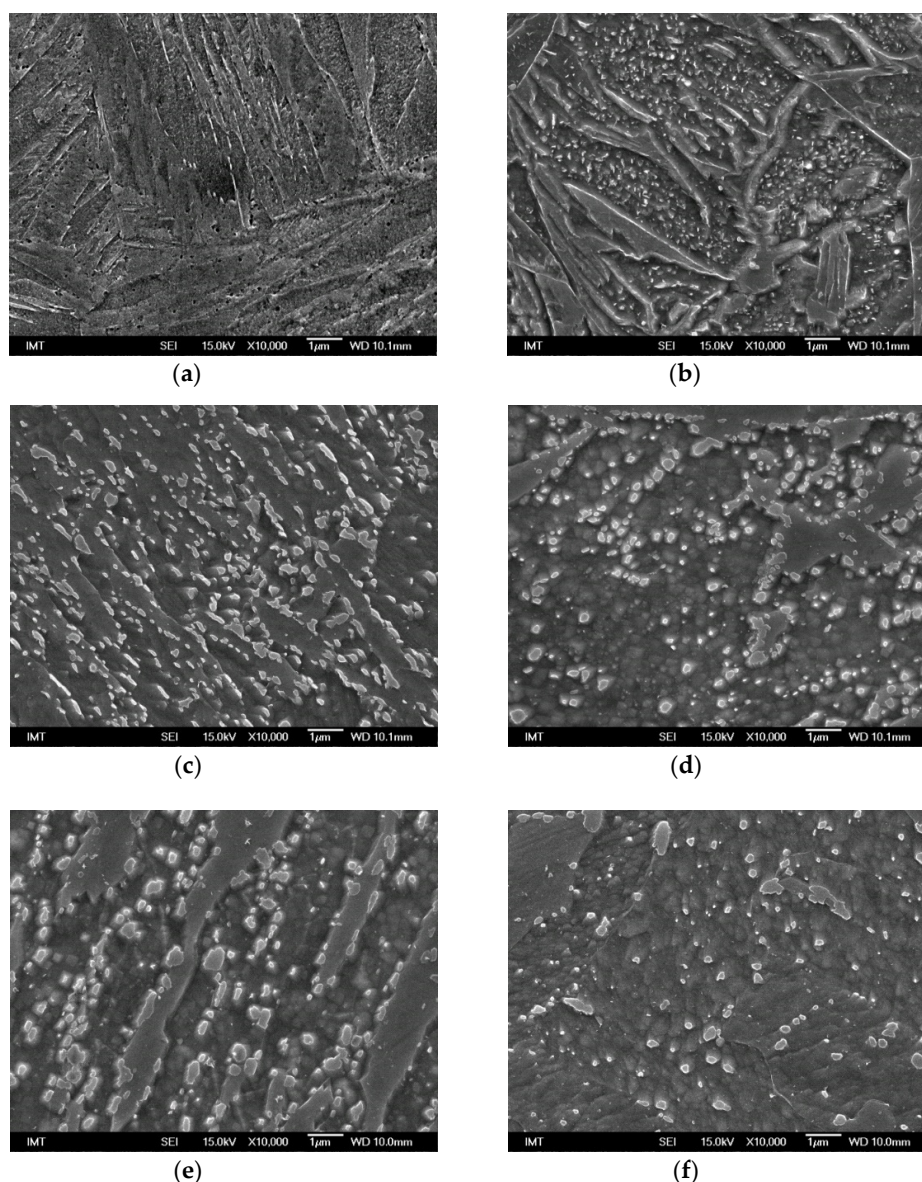


Figure 4. SEM micrographs of the coarse-grained (γ) HAZ microstructures of X20 and P91 steels for (a,b) initial state, (c,d) after tempering for 720 h at 650 °C, (e,f) after tempering for 720 h at 750 °C. Micrographs were previously published by the present authors in [36].

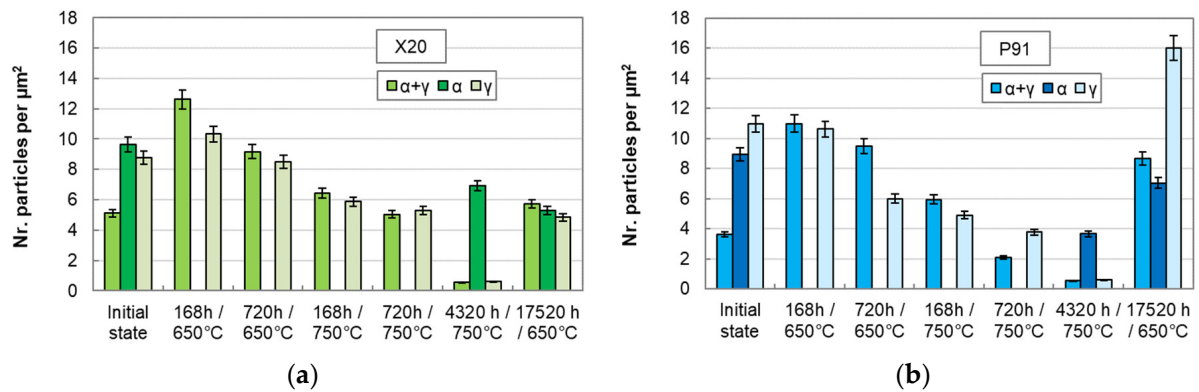


Figure 5. Number of precipitates per μm^2 for $\alpha + \gamma$, α , and γ microstructures of (a) X20 and (b) P91 steel in their initial state and after aging.

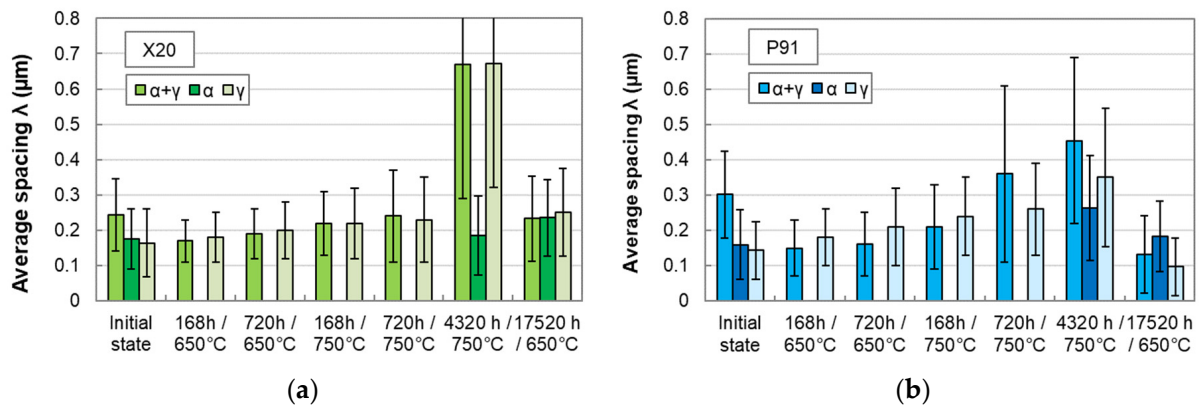


Figure 6. Average spacing of precipitates for $\alpha + \gamma$, α , and γ microstructures of (a) X20 and (b) P91 steel in their initial state and after aging.

2.3. Test Procedures

2.3.1. Accelerated Creep Tests

Accelerated creep tests using in-house designed creep-testing equipment with constant load and dead-weight lever arm were performed according to the ISO 204:2018 standard by applying a tensile stress of 170 MPa at the constant temperature of 580 °C lasting up to 100 h, with some exceptions where specimens ruptured earlier, depending on the microstructure. Detailed description of the accelerated creep tests can be found elsewhere [9,25,26]. In the accelerated creep tests and microstructure analyses, one sample from each tempering state was tested.

2.3.2. Friction Tests

Friction tests were performed on an oscillating tribological test rig (SRV4, Optimol Instruments Prüftechnik GmbH, Germany) with a ball-on-flat testing geometry using DIN 100Cr6 steel (AISI 52100 equivalent) balls with a diameter of 10 mm, sliding against the flat side of a half-cylinder. The balls had a hardness of 62.5 ± 2 HRC (corresponds to approximately 760 HV) and a roughness of $R_a 0.02 \mu\text{m}$. The initial hardness of the steels X20 and P91 was significantly lower than the hardness of the ball and had values of 238 HV and 228 HV, respectively.

To compare the frictional properties of the selected microstructures without and with the presence of oxides on the contacting surfaces, friction tests were performed under Ar atmosphere and in air. In air, metallic surfaces are covered with a thin layer of oxides which usually possess more favorable tribological properties than non-oxidized metallic surfaces [42]. The properties of nascent, non-oxidized metallic surfaces can be studied only in non-reactive atmospheres such as Ar, where the oxide layers cannot reform after

removal (due to the high reactivity of nascent metallic surfaces, oxide layers normally form very rapidly, e.g., 10^{-2} s at a pressure of 10^{-4} Torr [43]).

Before starting the friction tests, a flow of Ar gas with a gas pressure of 0.05 bar (g) at the gas-bottle outflow was directed onto the contact for 3 min to remove any adsorbed atmospheric contaminations. After 3 min of flushing with Ar gas, the friction test was started and after 2 min of sliding, Ar gas flow was stopped so that air could come into the contact. Afterwards, the test was conducted for an additional duration of 2 min. This way, around 10 cycles were performed under Ar stream flow and around 10 sliding cycles were performed in air.

Tests were performed at ambient temperature of 20 °C. The frequency of the oscillating motion was 0.125 Hz with amplitude of 2 mm resulting in a maximum sliding velocity of 1.6 mm/s (ball movement is sinusoidal). A normal load of 30 N was applied, corresponding to 0.98 GPa and 1.46 GPa of mean and maximal Hertzian contact pressures, respectively. The coefficient of friction was calculated as the ratio of the tangential force (friction force) and the normal force. The maximum coefficient of friction occurred at the beginning of each stroke, where a break-away friction was typically observed. This maximum value corresponds to the so-called static coefficient of friction and was regarded as the coefficient of friction of interest. Due to the high adhesion between the ball and the flat surface, the ball did not always return into its initial position although the ball holder did. Hence, due to the residual stresses between the ball holder and the ball, coefficient of friction was not zero, but gradually decreased to zero as the ball was slowly dragged into its initial position, which typically required 2–3 s after the end of an oscillating cycle. Therefore, after each oscillating cycle a waiting time of 12 s was applied.

Each microstructure was tested three times to ensure the repeatability of the measured friction curves.

2.3.3. Wear Tests

Wear tests were conducted immediately after the friction tests on the same oscillating tribological test rig and using the same samples. Since in an actual application, e.g., in fossil-fuel power plants, the majority of sliding wear is not expected to occur during regular operation at high temperatures but rather in special cases such as cold starts where the operating temperature is lower—for a typical cold start, the rotor surface and bore temperatures are near room temperature [44]—the wear behavior under ambient temperature was of primary interest. Therefore, the sliding wear experiments were conducted under ambient temperature conditions at 293.15 K (20 °C). The test duration was set to 15 min and the sliding frequency of 20 Hz was applied at a stroke of 2 mm, resulting in a maximal sliding velocity of 126 mm/s and a sliding distance of 72 m. Normal load of 30 N was applied, corresponding to 0.98 GPa of mean Hertzian contact pressure and 1.46 GPa of maximal Hertzian contact pressure. It should be noted that the calculated Hertzian contact is significantly higher than the yield strength of both materials and does not correspond to the actual contact pressure. Namely, the Hertzian contact pressure considers only the elastic deformation of the material; hence, when the yield strength of the material is exceeded, the actual contact pressure does not continue to increase exponentially but remains constant due to the plastic flow of the material and the related increase of the contact surface.

All tests were performed under dry sliding conditions, i.e., without any lubricant in the contact. Each experiment was repeated three times to ensure statistically relevant results.

After the wear tests, topographies of worn specimens were characterized using a white-light confocal microscope (μ surf, NanoFocus AG, Germany). From the topography data of the wear scars, wear volumes were calculated and subsequently specific wear rate coefficients were obtained by considering the Archard's law (Equation (1)) [45]:

$$k = \frac{V}{F \cdot s'} \quad (1)$$

where k is the specific wear rate coefficient in mm^3/Nm , V is the wear volume in mm^3 , F is the applied normal load in N, and s is the sliding distance in m.

The parameters applied in wear and friction tests are listed in Table 2.

Table 2. Parameters applied in wear and friction tests.

Parameter	Wear Tests	Friction Tests
Normal force (N)	30	30
Hertzian contact pressure (GPa)	0.98 (mean), 1.46 (maximum)	0.98 (mean), 1.46 (maximum)
Oscillation frequency (Hz)	20	0.125
Oscillation amplitude (mm)	2	2
Maximum velocity (mm/s)	126	1.6
Duration (min)	15	4
Number of cycles	18,000	20
Temperature ($^{\circ}\text{C}$)	24 (ambient temperature)	24 (ambient temperature)
Interfacial medium	none (dry)	none (dry)
Atmosphere	Air	Ar (2 min), air (2 min)

3. Results

3.1. Initial State (Influence of Microstructure/Grain Size)

Primary creep strain and secondary creep rate values of three different microstructures of the X20 and P91 steels at the initial state are shown in Figure 7. In Figure 7a, primary creep values are presented. In Figure 7a in the X20 steel, the primary creep strain decreased with the grain size and was the highest for the $\alpha + \gamma$ microstructure, slightly lower for the α microstructure and the lowest for the γ microstructure with the values of 0.04, 0.02, and 0.01 for $\alpha + \gamma$, α , and γ , respectively. In the P91 steel, the influence of grain size was not as straightforward; however, the lowest creep strain was obtained for the γ microstructure where a value of 0.003 was measured. The highest creep strain was measured for α microstructure with a value of 0.016, while in $\alpha + \gamma$ microstructure, creep strain was slightly lower with a value of 0.01. In Figure 7b, stationary (secondary) creep rate values are presented. In the X20 steel, the creep rate decreased with the grain size, similarly to the primary creep strain. The measured creep rate values were 2.2×10^{-4} h, 1.5×10^{-4} h, and 0.45×10^{-4} h for $\alpha + \gamma$, α , and γ , respectively. In P91 steel, the creep rate was the lowest for the γ microstructure where a value of 0.04×10^{-4} h was measured, while for $\alpha + \gamma$ and α microstructures, similar values of around 0.65×10^{-4} h were obtained. In Figure 7 it can also be seen that for both primary and stationary creep, the P91 steel provided lower creep strain and creep rate values than the X20 steel.

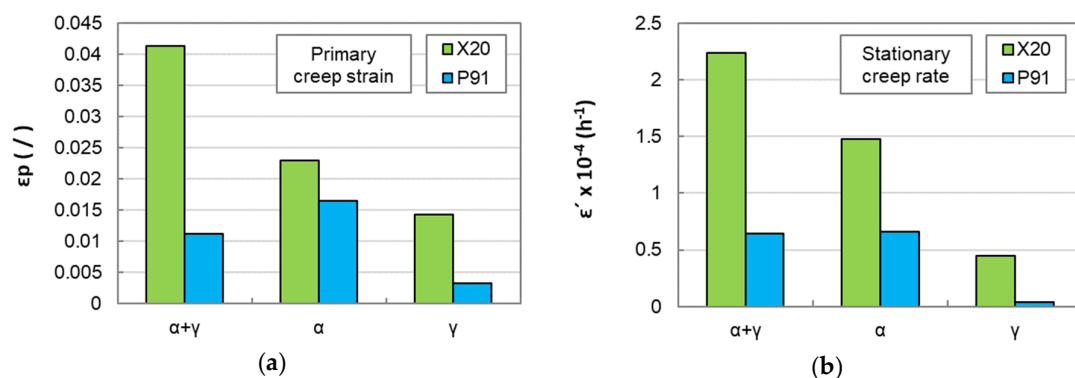


Figure 7. Creep performance of $\alpha + \gamma$, α , and γ microstructures of the X20 and P91 steels at the initial state: (a) primary creep strain, (b) stationary (secondary) creep rate.

Figure 8 shows static coefficients of friction of three different microstructures of the X20 and P91 steels at the initial state measured in Ar (Figure 8a) and air (Figure 8b) atmospheres.

In Figure 8, for both steels, coefficients of friction were higher in Ar atmosphere (Figure 8a) where values between 1.9 and 2.3 were measured, while in air atmosphere (Figure 8b), values between 1.4 and 1.9 were measured. It should be pointed out for all samples, that during the first few sliding cycles in Ar atmosphere, significantly lower friction values (0.3 to 1) were measured [37]. This shows that the surfaces were initially covered with a frictionally favorable oxide layer, which was quickly removed due to sliding under high contact pressure. Thus, the high friction values in Ar atmosphere can be attributed to the absence of any reactive molecules in the contact which could prevent from a direct steel/steel contact leading to the very high metal–metal adhesion and the consequent cold-welding of the asperities of contacting bodies [46]. On the other hand, the coefficient of friction values in air atmosphere are unusually high (based on previous studies of the present authors [21,25], values of around 1 were expected), which could be attributed to the fact that (i) the surfaces were roughened during the test in Ar atmosphere which led to mechanical anchoring of the asperities and/or (ii) the nascent steel surfaces from the test in Ar atmosphere could not fully re-oxidize within the relatively short test time in air (2 min).

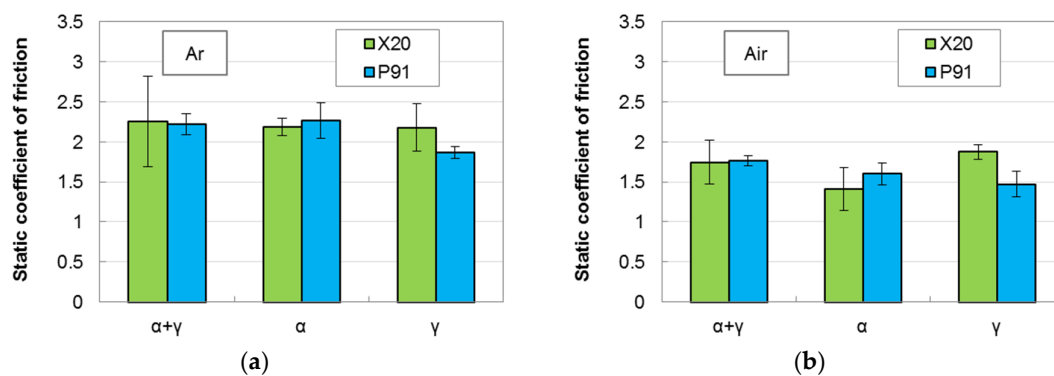


Figure 8. Static coefficients of friction of $\alpha + \gamma$, α , and γ microstructures of the X20 and P91 steels at the initial state. Tests were conducted under (a) Ar and (b) air atmospheres.

In Ar, the microstructures of both steels provided similar coefficient of friction values of around 2.2. The only exception was the P91 γ microstructure with around a 15% lower coefficient of friction at 1.9. In air, the lowest coefficient of friction with a value of 1.4 was measured for α microstructure of the X20 steel; it was around 20% lower than that of $\alpha + \gamma$ and γ microstructures having values of 1.8 and 1.9, respectively. For the P91 steel in air, coefficient of friction decreased with heat-treatment temperature and/or grain size: the lowest value of 1.5 was measured for γ microstructure; it was slightly higher for α microstructure with a value of 1.6 and the highest for $\alpha + \gamma$ microstructure where a value of 1.8 was measured.

In Figure 9, a steel specimen after the wear test is presented and Figure 10 shows specific wear rate coefficients of three different microstructures of the X20 and P91 steels at the initial state. In Figure 10, for the X20 steel wear rate decreased with heat-treatment temperature and/or grain size and had values of $1.6 \times 10^{-4} \text{ mm}^3/\text{Nm}$, $1.15 \times 10^{-4} \text{ mm}^3/\text{Nm}$ and $5 \times 10^{-5} \text{ mm}^3/\text{Nm}$ for $\alpha + \gamma$, α , and γ microstructures, respectively. For the P91 steel, the wear rate was the highest for $\alpha + \gamma$ microstructure with a value of $2.2 \times 10^{-4} \text{ mm}^3/\text{Nm}$ and the lowest for α microstructure with a value of $1.8 \times 10^{-4} \text{ mm}^3/\text{Nm}$. For γ microstructure, a value of $1.9 \times 10^{-4} \text{ mm}^3/\text{Nm}$ was measured and was therefore slightly higher than for α microstructure.

In Figure 10, it is also clear that at the initial state, wear rate was significantly lower for the X20 than for the P91 steel.

In Figure 7, Figure 8, and Figure 10, at the initial state, larger grain size provided a beneficial effect for creep, wear, and friction values of all tested samples. For coefficient of friction, this effect was observed only for the P91 steel—especially in air and partly in Ar atmosphere.

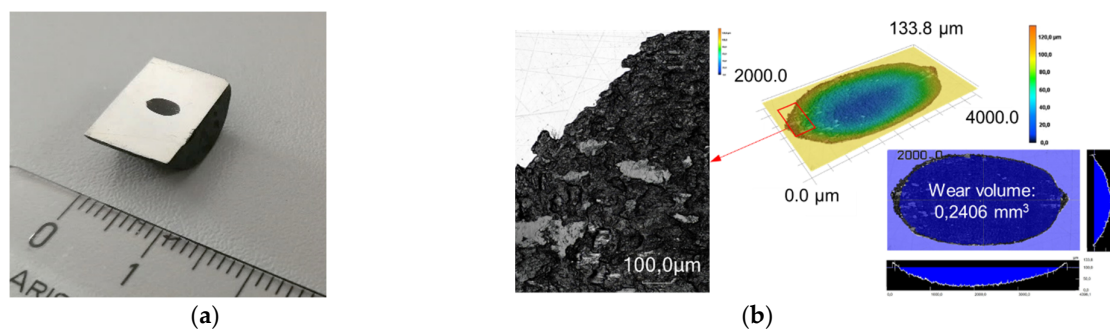


Figure 9. Steel specimen after the wear test: (a) visual appearance (b) assessment of the wear volume.

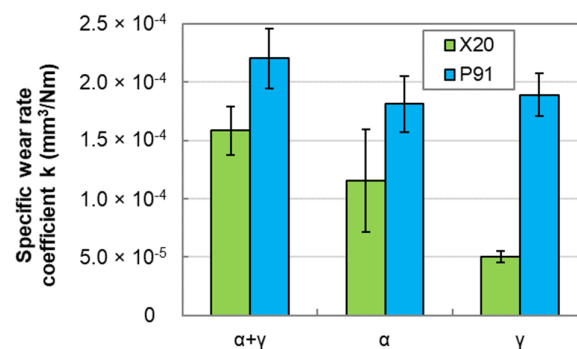


Figure 10. Specific wear rate coefficients of $\alpha + \gamma$, α , and γ microstructures of the X20 and P91 steels at the initial state.

3.2. After Aging (Influence of Precipitates Coarsening)

In Figure 11, primary creep strain values of three different microstructures of the X20 and P91 steels after aging for 17,520 h at 650 °C (Figure 11a) and 4320 h at 750 °C (Figure 11b) are shown. In Figure 11a, after aging for 17,520 h at 650 °C, primary creep strain was always higher for the X20 steel than for the P91 steel. For the X20 steel, the creep strain of $\alpha + \gamma$ and α microstructures was 0.03, while for γ microstructure it was around 30% lower, having a value of 0.02. For the P91 steel, all microstructures provided identical creep strain of 0.01. With aging for 4320 h at 750 °C (Figure 11b), for the X20 steel, creep strain was the lowest for α , slightly higher for $\alpha + \gamma$, and the highest for γ microstructure with values of 0.01, 0.02, and 0.03, respectively. For the P91 steel, creep strain of $\alpha + \gamma$ and α microstructures was 0.02, while for γ microstructure it was 50% lower, having a value of 0.01.

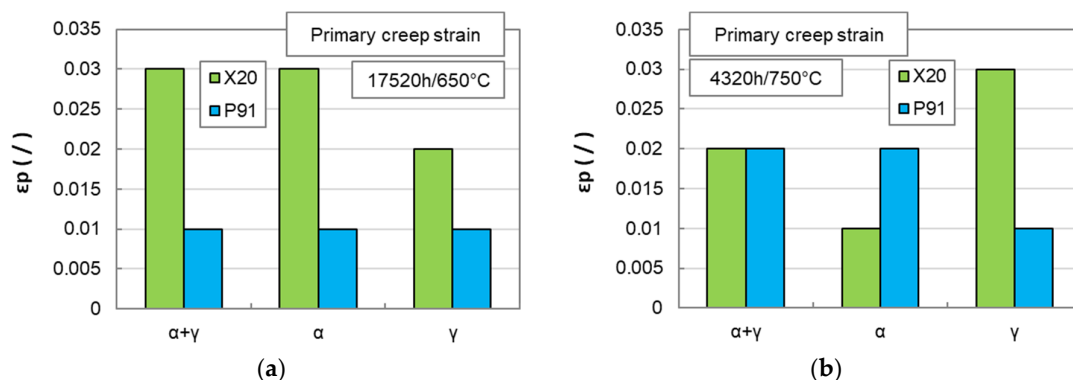


Figure 11. Primary creep strain values of $\alpha + \gamma$, α , and γ microstructures of the X20 and P91 steels after aging for (a) 17,520 h at 650 °C and (b) 4320 h at 750 °C.

From Figure 11, it is also clear that with aging for shorter time at the higher temperature (4320 h at 750 °C, Figure 11b), α and $\alpha + \gamma$ microstructures of the X20 steel

showed lower primary creep strain compared to longer aging time at the lower temperature (17,520 h at 650 °C, Figure 11a), while γ microstructure showed a higher primary creep strain. For the P91 steel, aging for shorter time at the higher temperature (4320 h at 750 °C, Figure 11b) increased the primary creep strain of α and $\alpha + \gamma$ microstructures, while it had no influence on γ microstructure.

Different creep behavior of both steels and the different influence of aging time and temperature come from the difference in chemical composition of the steels, which among other things leads to different precipitates morphology, thermodynamics, and kinetics [30]. Namely, as can be seen from Figures 5 and 6, the number of precipitates was always higher for the X20 steel compared to the P91 steel, resulting in larger average spacing of precipitates in the P91 steel. This is because the X20 steel has higher Cr and C content as compared to the P91 steel, which results in faster precipitation kinetics of the major type of precipitates in both steels ($Cr_{23}C_6$) for the same temperature-dependent diffusion conditions [30].

Compared to the initial state (Figure 7a), after aging the X20 steel, primary creep strain of $\alpha + \gamma$ microstructure decreased, while it increased for γ microstructure (Figure 11). For α microstructure, primary creep strain increased after aging for 17,520 h at 650 °C (Figure 11a), while it decreased after aging for 4320 h at 750 °C (Figure 11b). For the P91 steel, after aging for 17,520 h at 650 °C (Figure 11a), primary creep strain decreased for $\alpha + \gamma$ and α microstructures, while it increased for γ microstructure. After aging for 4320 h at 750 °C (Figure 11b), primary creep rate of all microstructures of the P91 steel increased as compared to the initial state (Figure 7a).

In Figure 12, stationary creep rate values of three different microstructures of the X20 and P91 steels after aging for 17,520 h at 650 °C (Figure 12a) and 4320 h at 750 °C (Figure 12b) are shown. It should be noted that in Figure 12a, the scale on the y-axis is 10-times smaller compared to Figure 12b. Generally, for stationary creep rate, similar trends were observed as for primary creep strain in Figure 11. Namely, stationary creep rate was always higher for the X20 steel than for the P91 steel, which was especially pronounced after aging for 17,520 h at 650 °C (Figure 12a). After aging for 17,520 h at 650 °C, the stationary creep rate was the highest for $\alpha + \gamma$ microstructure of the X20 steel with a value of 7.5×10^{-4} h, was around 35% lower for α with a creep rate of 4.7×10^{-4} h, and was the lowest for γ microstructure with a creep rate value of 2.6×10^{-4} h. For the P91 steel, the same trend was observed as for the X20 steel, with $\alpha + \gamma$ microstructure having the highest and γ microstructure the lowest creep rate; however, compared to the X20 steel, the wear rates were around 90% lower. After aging for 4320 h at 750 °C (Figure 12b), for the X20 steel, stationary creep rate was the lowest for α having a value of 32×10^{-4} h, while it was more than 2-times higher for $\alpha + \gamma$ and γ microstructures with values of 78×10^{-4} h and 72×10^{-4} h, respectively. For the P91 steel, creep rate was the lowest for γ and the highest for $\alpha + \gamma$ microstructure, and the creep rate values were 50 to 85% lower than in the X20 steel.

As can be seen in Figure 12, the effect of aging time and temperature on stationary creep rate of both steels was similar. Namely, for both steels aging for shorter time at the higher temperature (4320 h at 750 °C, Figure 12b) yielded significantly higher stationary creep rate values as compared to aging for longer time at the lower temperature (17,520 h at 650 °C, Figure 12a). The increase was more pronounced for the P91 steel where after shorter aging time at the higher temperature, 24 to 55-times higher stationary creep rates than after longer aging time at the lower temperature were measured, while in the X20 steel the increase was 6 to 27-fold.

Compared to the initial state (Figure 7b), after aging, the stationary creep rate of both steels increased. This was especially pronounced after aging for 4320 h at 750 °C (Figure 12b) where 20 to 160-times and 16 to 260-times higher creep rates as compared to the initial state were observed for the X20 and P91 steels, respectively. Aging for 17,520 h at 650 °C (Figure 12a) increased the stationary creep rate of the X20 steel for only 2 to 5-times as compared to the initial state, while in the case of the P91 steel in $\alpha + \gamma$ and α microstructures

no increase of the stationary creep rate was observed and in γ microstructure a 5-time increase as compared to the initial state was observed. For both steels after both aging conditions, the most and the least pronounced increases of the stationary creep rate as compared to the initial state were observed for γ and α microstructures, respectively.

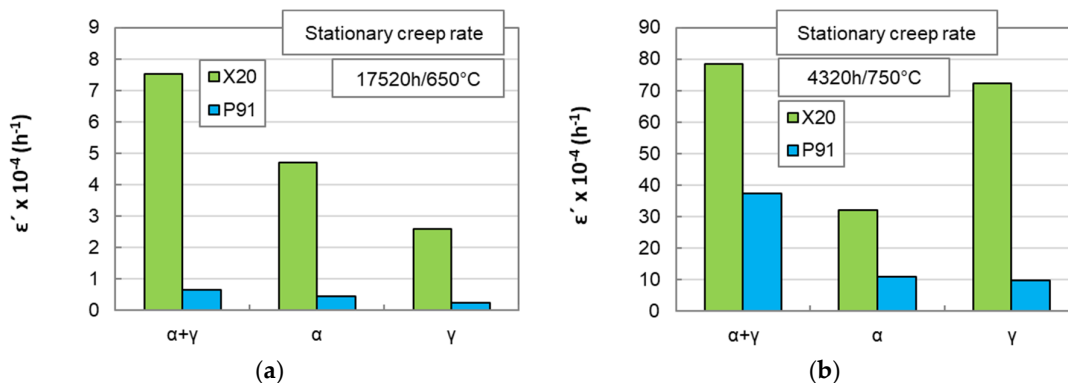


Figure 12. Stationary creep rate values of $\alpha + \gamma$, α , and γ microstructures of the X20 and P91 steels after aging for (a) 17,520 h at 650 °C and (b) 4320 h at 750 °C. In (a), the scale on the y-axis is 10-times smaller compared to (b).

In Figure 13, static coefficients of friction in Ar atmosphere for $\alpha + \gamma$ and γ microstructures of the X20 and P91 steels after aging for 168 h at 650 °C (Figure 13a) and 720 h at 750 °C (Figure 13b) are shown. In Figure 13, in Ar atmosphere, both microstructures of both steels provided almost identical coefficients of friction of around 2.7. Comparing to the initial state where values of around 2.2 were measured (Figure 8a), this is an increase of around 20%. It should be noted that only after aging for 720 h at 650 °C (not shown in the manuscript), γ microstructure of the P91 steel provided a slightly lower coefficient of friction of 2.5, which is in correlation with the lower coefficient of friction of this microstructure at the initial state (Figure 8a).

In Figure 14, static coefficients of friction in air atmosphere for $\alpha + \gamma$ and γ microstructures of the X20 and P91 steels after aging for 168 h at 650 °C (Figure 14a) and 720 h at 750 °C (Figure 14b) are shown. In Figure 14, coefficient of friction values in air atmosphere were only slightly lower (around 20 to 30%) as compared to Ar atmosphere (Figure 13), which was observed already for the microstructures at the initial state (Figure 8). After aging for 168 h at 650 °C (Figure 14a), $\alpha + \gamma$ microstructures of both steels provided slightly lower friction values than γ microstructures, while no significant difference between both steels was observed. After aging for 720 h at 750 °C (Figure 14b), $\alpha + \gamma$ microstructure of the P91 steel provided slightly higher friction values as compared to aging for 168 h at 650 °C, while other microstructures showed no notable differences.

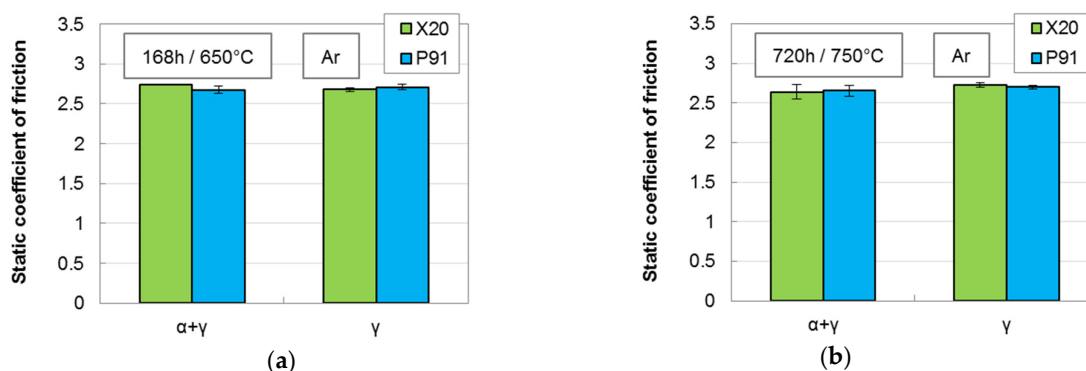


Figure 13. Static coefficients of friction in Ar atmosphere of $\alpha + \gamma$ and γ microstructures of the X20 and P91 steels after aging for (a) 168 h at 650 °C and (b) 720 h at 750 °C.

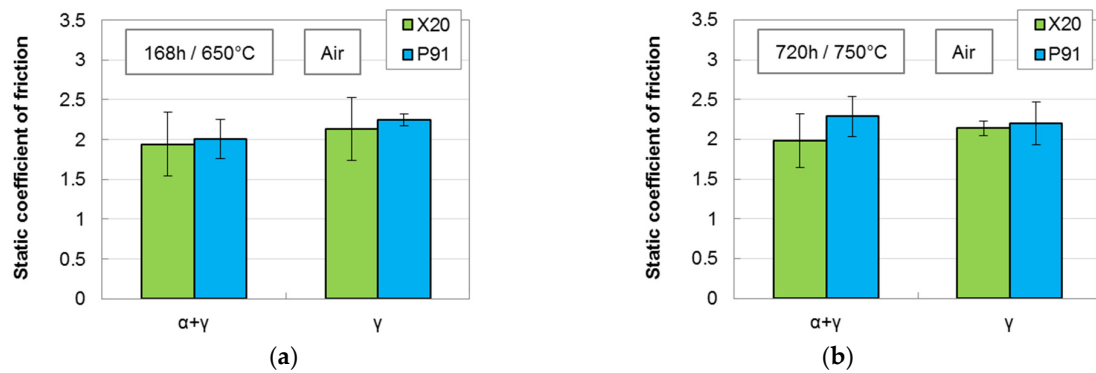


Figure 14. Static coefficients of friction in air atmosphere of $\alpha + \gamma$ and γ microstructures of the X20 and P91 steels after aging for (a) 168 h at 650 °C and (b) 720 h at 750 °C.

In Figure 15, specific wear rate coefficients of $\alpha + \gamma$ and γ microstructures of the X20 and P91 steels after aging for 168 h at 650 °C (Figure 15a) and 720 h at 750 °C (Figure 15b) are shown. In Figure 15, at both aging conditions, the wear of the P91 steel was higher as compared to the X20 steel; the only exception being $\alpha + \gamma$ microstructure after aging for 168 h at 650 °C, where both steels provided similar wear rates. It is interesting to note that the response of $\alpha + \gamma$ and γ microstructures to aging was inversely different for both steels. Namely, for the X20 steel after aging for 168 h at 650 °C, wear of $\alpha + \gamma$ microstructure was higher as compared to the γ microstructure, while it was the opposite after aging for 720 h at 750 °C. On the other hand, for the P91 steel, exactly the opposite trend was observed: after aging for 168 h at 650 °C, wear of $\alpha + \gamma$ microstructure was lower as compared to γ microstructure, while it was the opposite after aging for 720 h at 750 °C (Figure 15b).

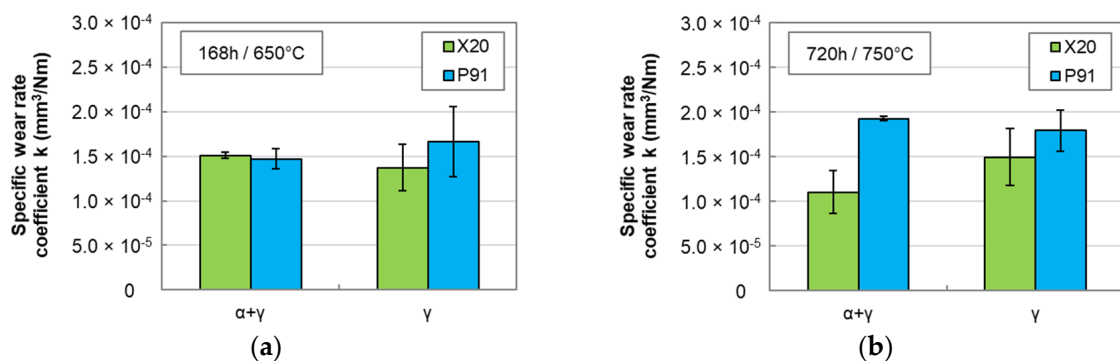


Figure 15. Specific wear rate coefficients of $\alpha + \gamma$ and γ microstructures of the X20 and P91 steels after aging for (a) 168 h at 650 °C and (b) 720 h at 750 °C.

4. Discussion

In Figure 16, static coefficients of friction in air atmosphere (Figure 16a,b), specific wear rate coefficients (Figure 16c,d), primary creep strain (Figure 16e,f), and stationary creep rate values (Figure 16g,h) for $\alpha + \gamma$, α , and γ microstructures of the X20 and P91 steels are presented in dependence of number of precipitates.

In Figure 16a,b, it can be observed that for both steels, static coefficients of friction in air atmosphere were slightly decreasing with increased number of precipitates. This was more pronounced in the P91 steel, where for the highest number of precipitates' coefficient of friction was around 30% lower as compared to the lowest number of precipitates. At the same time, for the P91 steel, a much higher fluctuation in coefficient of friction values was observed compared to the X20 steel. For the P91 steel, the difference between the highest and the lowest coefficient of friction was 37%, while it was only 16% for the X20 steel. Furthermore, for the P91 steel, coefficients of friction are slightly higher than for the X20 steel.

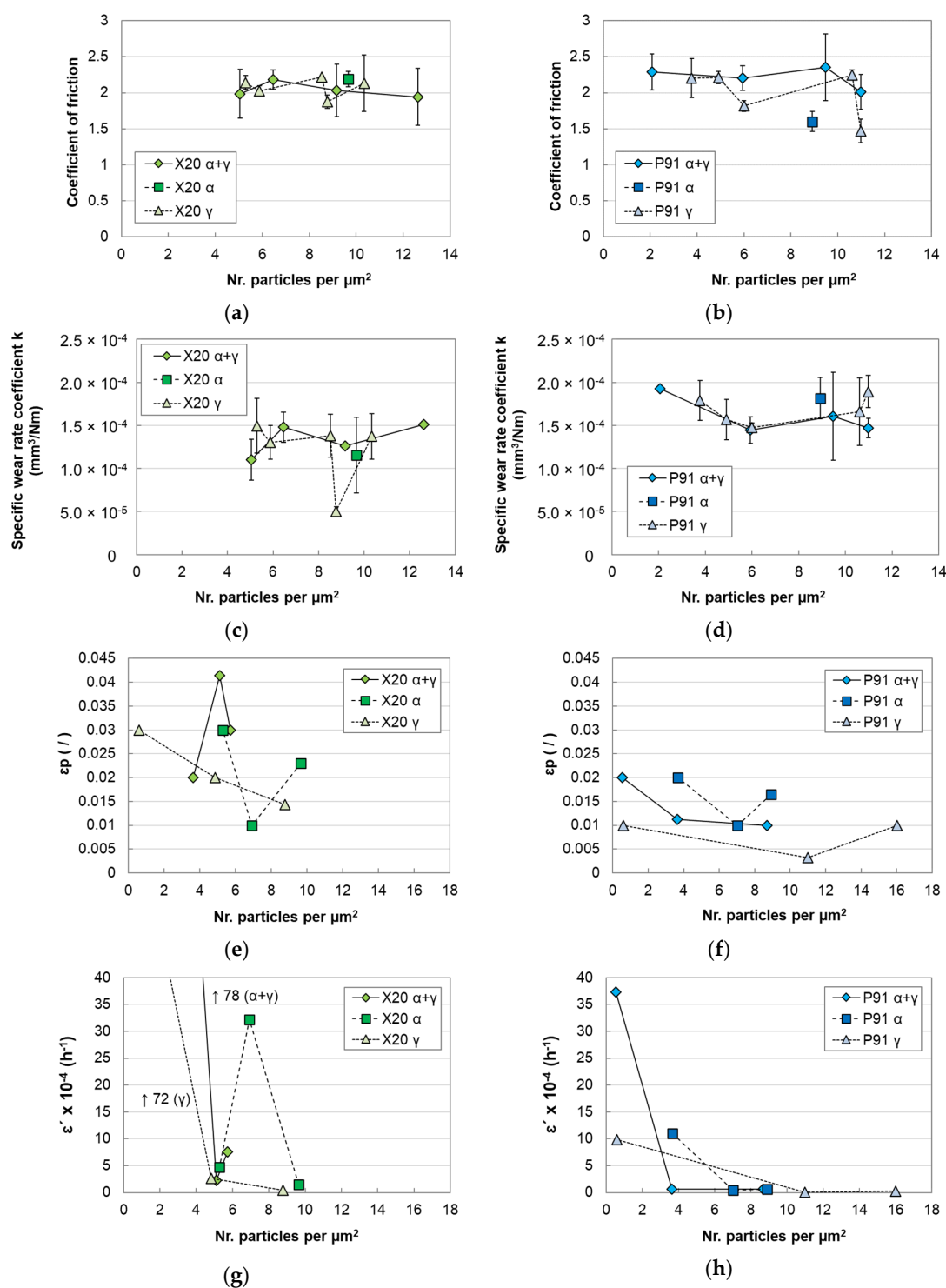


Figure 16. (a,b) Static coefficients of friction in air atmosphere, (c,d) specific wear rate coefficients, (e,f) primary creep strain, and (g,h) stationary creep rate values of $\alpha + \gamma$, α , and γ microstructures of the X20 and P91 steels in dependence of number of precipitates. In (a–d), the scale on the x-axis is different compared to (e–h).

In Figure 16c,d, for both steels, the minimum wear was reached at an approximately intermediate number of precipitates. For the X20 steel, this was at around 9 precipitates per μm^2 , while for the P91 steel, it was at around 6 precipitates per μm^2 . However, both steels showed a slightly different wear behavior in relation to the number of precipitates. For the X20 steel, at the lowest number of precipitates, relatively low wear values were measured, which were also lower compared to the wear values at the highest number of precipitates.

On the other hand, for the P91 steel, at the lowest number of precipitates, the highest wear values were measured and at the highest number of precipitates, wear values were generally low, but had a high fluctuation in measured values depending on the type of the microstructure ($\alpha + \gamma$, α , and γ). Similar as for coefficients of friction (Figure 16a,b), for the X20 steel, the wear values were slightly lower than for the P91 steel; however, the difference between the minimum and the maximum wear value was higher for the X20 steel.

In Figure 16e,f, for both steels, primary creep strain initially decreased with increasing number of precipitates and at the highest number of precipitates, it started to increase. For both steels, the lowest creep strains were obtained in the range of 7 to 11 precipitates per μm^2 . Generally, the P91 steel provided lower primary creep strain values compared to the X20 steel. For the X20 steel, the primary creep strain of $\alpha + \gamma$ microstructure initially increased and afterwards decreased with the number of precipitates. For α microstructure, it initially decreased and afterwards increased, while for γ microstructure it always decreased with the number of precipitates. For the P91 steel, the primary creep strain of $\alpha + \gamma$ microstructure always decreased with the number of precipitates, while for α and γ microstructures it initially decreased and afterwards increased with the number of precipitates. For both steels, for similar number of precipitates, γ microstructure generally provided lower primary creep strain values than α and $\alpha + \gamma$ microstructures. For the P91 steel, the lowest primary creep strain also was obtained in γ microstructure, while for the X20 steel the lowest primary creep strain was obtained in α microstructure.

In Figure 16g,h, for both steels, the stationary creep rate significantly decreased in the range of around 0.5 to 6 precipitates per μm^2 . For the X20 steel, where generally higher stationary creep rate values were obtained, for $\mu + \gamma$ and γ microstructures stationary creep rate decreased from over 70×10^{-4} at around 0.5 precipitates per μm^2 to around 2.5×10^{-4} at around 5 precipitates per μm^2 (more than a 25-fold decrease). On the other hand, for the P91 steel, where generally lower stationary creep rate values were obtained, the maximal measured stationary creep rate ($\alpha + \gamma$ microstructure) decreased from 37×10^{-4} at around 0.5 precipitates per μm^2 to around 5×10^{-5} at around 4 precipitates per μm^2 (more than a 70-fold decrease). For both steels, at more than 6 precipitates per μm^2 , no significant change in stationary creep rate value was observed. The exception was α microstructure of the X20 steel where at around 7 precipitates per μm^2 , a stationary creep rate of around 30×10^{-4} was measured.

In Figure 17, static coefficients of friction in air atmosphere (Figure 17a), specific wear rate coefficients (Figure 17b), and stationary creep rate values (Figure 17c) of $\alpha + \gamma$, α , and γ microstructures of the X20 and P91 steels are presented in dependence of number of precipitates. For reference, the coefficient of friction data are fitted with a linear trendline, while specific wear rate coefficients and stationary creep rate values are fitted with a third order polynomial curve. In Figure 17, the trends due to precipitation can clearly be seen. Coefficient of friction is approximately linearly decreasing with the increased number of precipitates (Figure 17a), while wear rate shows a decrease between 4 and 8 precipitates per μm^2 , where the wear rate starts to increase with increasing number of precipitates (Figure 17b). For the primary creep strain, no general trend related to the number of precipitates was observed. On the other hand, in the range of around 0.5 to 6 precipitates per μm^2 , the stationary creep rate (Figure 17c) significantly decreased (from over 70×10^{-4} to around 5×10^{-5}), while at a higher number of precipitates it remained very low (around 1×10^{-4} or lower) and no significant changes were observed.

The results from the present study correlate well with findings observed in other studies. For example, in [47] the effect of precipitated carbides on the friction coefficient and wear volume was analyzed. The results indicated that the carbides precipitated after aging treatment strongly affected the wear behavior during the fretting wear. Carbide precipitation slightly increased the friction coefficient and at the same time, the wear volume increased with increase of carbides. In [11], the influence of corrosion pits on the endurable fatigue loading in different environments and at various stress ratios was investigated for 12% Cr steam turbine blade steel. Two different batches of the same

material (403/410 12% Cr martensitic steel) were used. For the material with a higher number of inclusions, a significant decrease of the stress-life (S–N) curve was observed and inclusions were often observed at the crack initiation site of smooth specimens for both materials. Authors suggested that the probability of crack initiation is enhanced with an increased number of inclusions that are acting as stress raisers.

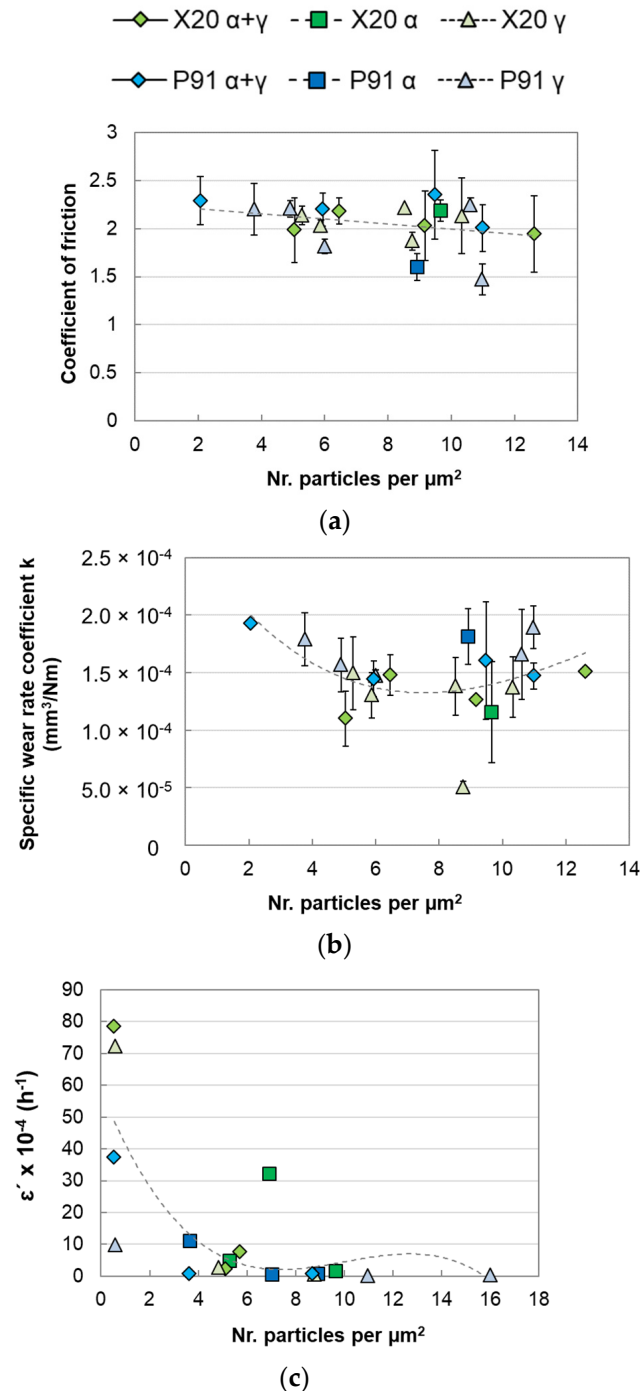


Figure 17. (a) Static coefficients of friction in air atmosphere, (b) specific wear rate coefficients, and (c) stationary creep rate values of $\alpha + \gamma$, α , and γ microstructures of the X20 and P91 steels in dependence of number of precipitates.

5. Conclusions

From the present study of two 9–12 wt.% Cr martensitic alloy steels, the X20 and P91, the following conclusions can be drawn:

1. Both prior to and after aging, the P91 steel typically provided significantly higher creep resistance than the X20 steel, while the latter provided slightly better tribological performance (lower friction and wear).
2. Prior to aging, the stationary creep rate, wear, and friction of both steels decreased with the increase in grain size, i.e., the values were typically the highest for $\alpha + \gamma$ and the lowest for γ microstructure.
3. After aging for a shorter time at higher temperature, $\alpha + \gamma$ and α microstructures of the X20 steel showed lower primary creep strain compared to longer aging time at lower temperature, while for γ microstructure of the X20 steel, an opposite trend was observed. On the other hand, for the P91 steel, aging for a shorter time at the higher temperature increased the primary creep strain of α and $\alpha + \gamma$ microstructures, while it had no influence on γ microstructure.
4. For both steels, aging for a shorter time at the higher temperature yielded significantly higher stationary creep rate values as compared to aging for a longer time at the lower temperature. The increase was more pronounced in the P91 than in the X20 steel.
5. For both steels, as a function of the increasing number of precipitates, static coefficient of friction in air atmosphere was approximately linearly decreasing, while the wear rate initially decreased, showed a minimum value at around 8 precipitates per μm^2 , and then started to increase.
6. For the primary creep strain, no general trend related to the number of precipitates was observed; however, for both steels, a significant decrease of the stationary creep rate was observed in the range of around 0.5 to 6 precipitates per μm^2 , while for higher number of precipitates, the stationary creep rates remained very low and no significant changes were observed.

Author Contributions: Conceptualization, I.V. and F.K.; methodology, I.V., F.K. and B.P.; investigation, I.V. and F.K.; writing—original draft preparation, I.V.; writing—review and editing, F.K. and J.V.; supervision, B.P. All authors have read and agreed to the published version of the manuscript.

Funding: This work was funded by the Austrian COMET Program (project K2 InTribology, no. 872176) and carried out at the “Excellence Centre of Tribology” AC2T research GmbH in cooperation with V-Research GmbH and Institute for Metals and Technology (IMT).

Data Availability Statement: Not applicable.

Acknowledgments: The authors would like to thank Stefan Klien and Alexander Diem for their contribution to the conceptualization and the experimental design of the present research.

Conflicts of Interest: The authors declare no conflict of interest. The funders had no role in the design of the study; in the collection, analyses, or interpretation of data; in the writing of the manuscript, or in the decision to publish the results.

References

1. Di Gianfrancesco, A.; Vipraio, S.T.; Venditti, D. Long Term Microstructural Evolution of 9–12%Cr Steel Grades for Steam Power Generation Plants. *Procedia Eng.* **2013**, *55*, 27–35. [[CrossRef](#)]
2. Xu, L.; Wang, B.; Zhu, J.; Li, W.; Zheng, Z. Effect of Cr content on the corrosion performance of low-Cr alloy steel in a CO₂ environment. *Appl. Surf. Sci.* **2016**, *379*, 39–46. [[CrossRef](#)]
3. Schönbauer, B.M.; Perlega, A.; Karr, U.P.; Gandy, D.; Stanzl-Tschegg, S.E. Pit-to-crack transition under cyclic loading in 12% Cr steam turbine blade steel. *Int. J. Fatigue* **2015**, *76*, 19–32. [[CrossRef](#)]
4. Metsäjoki, J.; Huttunen-Saarivirta, E.; Lepistö, T. Elevated-temperature corrosion of uncoated and aluminized 9–12% Cr boiler steels beneath KCl deposit. *Fuel* **2014**, *133*, 173–181. [[CrossRef](#)]
5. Hald, J. Microstructure and long-term creep properties of 9–12% Cr steels. *Int. J. Press. Vessel. Pip.* **2008**, *85*, 30–37. [[CrossRef](#)]
6. Abe, F. Precipitate design for creep strengthening of 9% Cr tempered martensitic steel for ultra-supercritical power plants. *Sci. Technol. Adv. Mater.* **2008**, *9*, 013002. [[CrossRef](#)]

7. Rojas, D.; Garcia, J.; Prat, O.; Sauthoff, G.; Kaysser-Pyzalla, A. 9%Cr heat resistant steels: Alloy design, microstructure evolution and creep response at 650 °C. *Mater. Sci. Eng. A* **2011**, *528*, 5164–5176. [[CrossRef](#)]
8. Yadav, S.D.; El-Tahawy, M.; Kalácska, S.; Dománková, M.; Yubero, D.C.; Poletti, C. Characterizing dislocation configurations and their evolution during creep of a new 12% Cr steel. *Mater. Charact.* **2017**, *134*, 387–397. [[CrossRef](#)]
9. Žužek, B.; Podgornik, B.; Kafexhiu, F. Development of microstructure and creep resistance of a martensitic creep resistant steel. *Int. J. Microstruct. Mater. Prop.* **2017**, *12*, 301. [[CrossRef](#)]
10. Lucacci, G. Steels and alloys for turbine blades in ultra-supercritical power plants. In *Materials for Ultra-Supercritical and Advanced Ultra-Supercritical Power Plants*; Elsevier BV: Amsterdam, The Netherlands, 2017; pp. 175–196.
11. Schönbauer, B.M.; Stanzl-Tschegg, S.E.; Perlega, A.; Salzman, R.N.; Rieger, N.F.; Zhou, S.; Turnbull, A.; Gandy, D. Fatigue life estimation of pitted 12% Cr steam turbine blade steel in different environments and at different stress ratios. *Int. J. Fatigue* **2014**, *65*, 33–43. [[CrossRef](#)]
12. Asai, K. Fretting fatigue strength of 12% Cr steel under high local contact pressure and its fracture mechanics analysis. *Procedia Eng.* **2010**, *2*, 475–484. [[CrossRef](#)]
13. Di Gianfrancesco, A. (Ed.) *Materials for Ultra-Supercritical and Advanced Ultra-Supercritical Power Plants*, 1st ed.; Woodhead Publishing series in energy; Woodhead Publishing: Cambridge, UK, 2016; ISBN 978-0-08-100558-3.
14. Peng, Y.-Q.; Chen, T.-C.; Chung, T.-J.; Jeng, S.-L.; Huang, R.-T.; Tsay, L.-W. Creep Rupture of the Simulated HAZ of T92 Steel Compared to that of a T91 Steel. *Materials* **2017**, *10*, 139. [[CrossRef](#)] [[PubMed](#)]
15. Shen, Y.; Chen, B.; Wang, C. In Situ Observation of Phase Transformations in the Coarse-Grained Heat-Affected Zone of P91 Heat-Resistant Steel During Simulated Welding Process. *Met. Mater. Trans. A* **2020**, *51*, 3371–3376. [[CrossRef](#)]
16. Mariappan, K.; Shankar, V.; Bhaduri, A.K. Comparative evaluation of tensile properties of simulated heat affected zones of P91 steel weld joint. *Mater. High Temp.* **2020**, *37*, 114–128. [[CrossRef](#)]
17. Yang, K.; Zhang, Y.; Zhao, J. Elastoplastic Fracture Analysis of the P91 Steel Welded Joint under Repair Welding Thermal Shock Based on XFEM. *Metals* **2020**, *10*, 1285. [[CrossRef](#)]
18. Lojen, G.; Vuherer, T. Optimization of PWHT of Simulated HAZ Subzones in P91 Steel with Respect to Hardness and Impact Toughness. *Metals* **2020**, *10*, 1215. [[CrossRef](#)]
19. Smith, A.; Asadikiya, M.; Yang, M.; Chen, J.; Zhong, Y. An Investigation of Creep Resistance in Grade 91 Steel through Computational Thermodynamics. *Engineering* **2020**, *6*, 644–652. [[CrossRef](#)]
20. Kafexhiu, F.; Burja, J. Evaluation of Stationary Creep Rate in Heat-Affected Zone of Martensitic 9–12% Cr Steels. *Metals* **2020**, *10*, 1612. [[CrossRef](#)]
21. Abson, D.J.; Rothwell, J.S. Review of type IV cracking of weldments in 9–12%Cr creep strength enhanced ferritic steels. *Int. Mater. Rev.* **2013**, *58*, 437–473. [[CrossRef](#)]
22. Mayr, P. *Evolution of Microstructure and Mechanical Properties of the Heat Affected Zone in B-Containing 9% Chromium Steels*; Graz University of Technology: Graz, Austria, 2007.
23. Cerjak, H.-H.; Mayr, P. Creep strength of welded joints of ferritic steels. In *Creep-Resistant Steels*; Abe, F., Kern, T.-U., Viswanathan, R., Eds.; Woodhead Publishing Limited: Cambridge, UK; CRC Press LLC: Boca Raton, FL, USA, 2008; pp. 472–503.
24. Cerjak, H.-H.; Holzer, I.; Mayr, P.; Pein, C.; Sonderegger, B.; Kozeschnik, E. The Relation between Microstructure and Creep Properties of Martensitic 9–12% Cr Steels. In *Proceedings of the New Developments on Metallurgy and Applications of High Strength Steels*, Buenos Aires, Argentina, 26–28 May 2008; pp. 247–265.
25. Kafexhiu, F.; Vodopivec, F.; Podgornik, B. Analysis of Primary Creep in Simulated Heat Affected Zone (HAZ) of Two 9–12% Cr Steel Grades. *Metalurgija* **2017**, *56*, 353–356.
26. Kafexhiu, F.; Podgornik, B.; Vodopivec, F. Ageing effect on the creep performance of simulated weld HAZ for the steels X20 and P91. *MATEC Web Conf.* **2018**, *188*, 03004. [[CrossRef](#)]
27. Skobir, D.A.; Vodopivec, F.; Kosec, L.; Jenko, M.; Vojvodič-Tuma, J. Influence of Precipitates Size and Distribution on Room Temperature Mechanical Properties and Accelerated Creep of X20CrMoV121. *Steel Res. Int.* **2004**, *75*, 196–203. [[CrossRef](#)]
28. Liu, X.; Fan, P.; Zhu, L. Characterization of dislocation evolution during creep of 9Cr 1Mo steel using internal friction measurement. *Mater. Charact.* **2019**, *150*, 98–106. [[CrossRef](#)]
29. Li, M.; Wang, L.; Almer, J.D. Dislocation evolution during tensile deformation in ferritic–martensitic steels revealed by high-energy X-rays. *Acta Mater.* **2014**, *76*, 381–393. [[CrossRef](#)]
30. Panait, C.G.; Zielińska-Lipiec, A.; Koziel, T.; Czyrska-Filemonowicz, A.; Gourgues-Lorenzon, A.-F.; Bendick, W. Evolution of dislocation density, size of subgrains and MX-type precipitates in a P91 steel during creep and during thermal ageing at 600C for more than 100,000h. *Mater. Sci. Eng. A* **2010**, *527*, 4062–4069. [[CrossRef](#)]
31. Morsdorf, L.; Jeannin, O.; Barbier, D.; Mitsuhashi, M.; Raabe, D.; Tasan, C. Multiple mechanisms of lath martensite plasticity. *Acta Mater.* **2016**, *121*, 202–214. [[CrossRef](#)]
32. Shibata, A.; Nagoshi, T.; Sone, M.; Morito, S.; Higo, Y. Evaluation of the block boundary and sub-block boundary strengths of ferrous lath martensite using a micro-bending test. *Mater. Sci. Eng. A* **2010**, *527*, 7538–7544. [[CrossRef](#)]
33. Morito, S.; Adachi, Y.; Ohba, T. Morphology and Crystallography of Sub-Blocks in Ultra-Low Carbon Lath Martensite Steel. *Mater. Trans.* **2009**, *50*, 1919–1923. [[CrossRef](#)]
34. Fedorova, I.; Belyakov, A.; Kozlov, P.; Skorobogatykh, V.; Shenkova, I.; Kaibyshev, R. Laves-phase precipitates in a low-carbon 9% Cr martensitic steel during aging and creep at 923 K. *Mater. Sci. Eng. A* **2014**, *615*, 153–163. [[CrossRef](#)]

35. Isik, M.; Kostka, A.; Yardley, V.; Pradeep, K.; Duarte, M.; Choi, P.; Raabe, D.; Eggeler, G. The nucleation of Mo-rich Laves phase particles adjacent to M₂₃C₆ micrograin boundary carbides in 12% Cr tempered martensite ferritic steels. *Acta Mater.* **2015**, *90*, 94–104. [[CrossRef](#)]
36. Velkavrh, I.; Kafexhiu, F.; Klien, S.; Diem, A.; Podgornik, B. Tempering-Induced Microstructural Changes in the Weld Heat-Affected Zone of 9 to 12 Pct Cr Steels and Their Influence on Sliding Wear. *Met. Mater. Trans. A* **2017**, *48*, 109–125. [[CrossRef](#)]
37. Velkavrh, I.; Kafexhiu, F.; Klien, S.; Ausserer, F.; Voyer, J.; Diem, A.; Podgornik, B. The influence of carbide coarsening on the friction properties of thermally affected 9–12 wt. % Cr steels. *J. Phys. Conf. Ser.* **2017**, *843*, 012065. [[CrossRef](#)]
38. Beausir, J.-J.F.B. *ATEX ©—Analysis Tools for Electron and X-ray Diffraction*; Université de Lorraine: Metz, France, 2017.
39. Altendorf, H.; Faessel, M.; Jeulin, D.; Latourte, F. Direct estimation of austenitic grain dimensions in heat affected zones of a martensitic steel from EBSD images. *J. Microsc.* **2015**, *258*, 87–104. [[CrossRef](#)] [[PubMed](#)]
40. GIMP—GNU Image Manipulation Program, Free Software. Available online: <https://www.gimp.org/> (accessed on 22 December 2020).
41. Schindelin, J.; Arganda-Carreras, I.; Frise, E.; Kaynig, V.; Longair, M.; Pietzsch, T.; Preibisch, S.; Rueden, C.; Saalfeld, S.; Schmid, B.; et al. Fiji: An open-source platform for biological-image analysis. *Nat. Methods* **2012**, *9*, 676–682. [[CrossRef](#)]
42. Velkavrh, I.; Ausserer, F.; Klien, S.; Voyer, J.; Ristow, A.; Brenner, J.; Forêt, P.; Diem, A. The influence of temperature on friction and wear of unlubricated steel/steel contacts in different gaseous atmospheres. *Tribol. Int.* **2016**, *98*, 155–171. [[CrossRef](#)]
43. Cabrera, N.; Mott, N.F. Theory of the oxidation of metals. *Rep. Prog. Phys.* **1949**, *12*, 163–184. [[CrossRef](#)]
44. Dinh, C.; Marriner, B.; Tadros, R.; Kim, S.Y.; Farineau, T. *Design and Operation of Large Fossil-Fueled Steam Turbines in Cyclic Duty*; General Electric Company: Boston, MA, USA, 2016; p. 9.
45. Archard, J.F. Contact and Rubbing of Flat Surfaces. *J. Appl. Phys.* **1953**, *24*, 981–988. [[CrossRef](#)]
46. Velkavrh, I.; Ausserer, F.; Klien, S.; Brenner, J.; Forêt, P.; Diem, A. The effect of gaseous atmospheres on friction and wear of steel–steel contacts. *Tribol. Int.* **2014**, *79*, 99–110. [[CrossRef](#)]
47. Zhang, H.; Lu, Y.; Ma, M.; Li, J. Effect of precipitated carbides on the fretting wear behavior of Inconel 600 alloy. *Wear* **2014**, *315*, 58–67. [[CrossRef](#)]